Robotics and Autonomous Systems 175 (2024) 104643

Contents lists available at ScienceDirect

Robotics and Autonomous Systems

journal homepage: www.elsevier.com/locate/robot

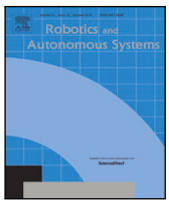

Modelling and identification methods for simulation of cable-suspended dual-arm robotic systems☆

Giancarlo D'Ago [a,b,*], Mario Selvaggio [b], Alejandro Suarez [c], Francisco Javier Gañán [c], Luca Rosario Buonocore [a], Mario Di Castro [a], Vincenzo Lippiello [b], Anibal Ollero [c], Fabio Ruggiero [b]

[a] European Organization for Nuclear Research, CERN, Espl. des Particules 1, Meyrin, 1211, Switzerland
[b] PRISMA Lab, Department of Electrical Engineering and Information Technology, University of Naples Federico II, Via Claudio 21, Naples, 80125, Italy
[c] GRVC Robotics Labs, University of Seville, Camino de los Descubrimientos, Seville, 41092, Spain

ARTICLE INFO

Keywords:
Robotics in Hazardous fields
Aerial systems
Applications

ABSTRACT

This paper proposes rigid-body modelling and identification procedures for long-reach dual-arm manipulators in a cable-suspended pendulum configuration. The proposed model relies on a virtually constrained open kinematic chain and lends itself to be simulated through the most commonly used robotic simulators without explicitly account for the cables constraints and flexibility. Moreover, a dynamic parameters identification procedure is devised to improve the simulation model fidelity and reduce the sim-to-real gap for controllers deployment. We show the capability of our model to handle different cable configurations and suspension mechanisms by customising it for two representative cable-suspended dual-arm manipulation systems: the LiCAS arms suspended by a drone and the CRANEbot system, featuring two Pilz arms suspended by a crane. The identified dynamic models are validated by comparing their evolution with data acquired from the real systems showing a high (between 91.3% to 99.4%) correlation of the response signals. In a comparison performed with baseline pendulum models, our model increases the simulation accuracy from 64.4% to 85.9%. The simulation environment and the related controllers are released as open-source code.

1. Introduction

Cable-suspended long-reach manipulators have classically being utilised to perform inspection and maintenance tasks over large but difficult-to-access workspaces in hazardous industrial scenarios. Only recently, their use has been extended to the execution of challenging operations in remote high-altitude areas (e.g., maintenance of power lines, inspection of remote infrastructures, etc.) where the direct access of humans is dangerous or costly [1–3]. These robots are typically constituted by a suspension platform that transports an articulated lower platform in a cable-suspended pendulum configuration, as shown in Fig. 1. One or multiple cables connect the two parts and are employed to: (i) decrease the weight of the overall robotic system compared to using rigid links; (ii) provide orders of magnitude larger end-effector workspace without affecting the weight of the manipulators' base; and (iii) exhibit superior resilience in absorbing external disturbances such as impacts and collisions. Long-reach aerial manipulators, equipped with flexible links or multi-cable structures, are being developed to additionally increase the distance between the aerial platform and the environmental obstacles, thus lowering down the risk of impacts of the rotor blades [4–7]. In this case, the presence of cables has minimal impact on the overall aerial robot weight and enables to safely operate in constrained environments without affecting its energetic autonomy level.

The accurate simulation and, consequently, the development and the deployment of model-based control strategies for cable-suspended long-reach manipulators, is hindered by the lack of models that accurately capture the system's behaviour. Indeed, despite the numerous advantages, the presence of passive cables generally makes the modelling of these robotic systems more involved, since low-mass and flexible elements introduce an uncontrolled second-order dynamics oscillatory behaviour and impose intricate unilateral constraints between the platforms. In aerial transportation of non-actuated loads through passive flexible links, the cable system is generally modelled as a single rigid link [9], by using finite elements methods [10],

☆ The research leading to these results has been supported by the AERIAL-CORE project (Horizon 2020 Grant Agreement No. 871479). The authors are solely responsible for its content.

* Corresponding author at: European Organization for Nuclear Research, CERN, Espl. des Particules 1, Meyrin, 1211, Switzerland.
E-mail address: giancarlo.dago@cern.ch (G. D'Ago).

https://doi.org/10.1016/j.robot.2024.104643
Received 17 October 2023; Received in revised form 5 January 2024; Accepted 25 January 2024
Available online 7 February 2024

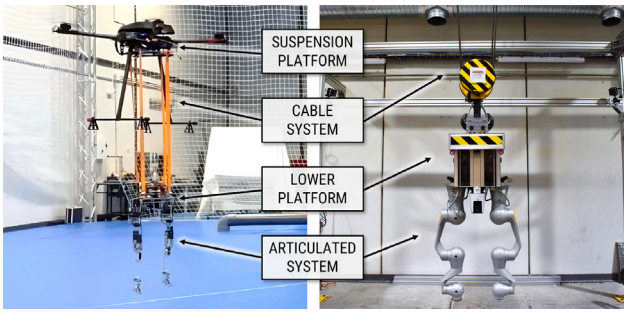

Fig. 1. The two dual-arm manipulation systems considered in this work as examples of cable-suspended robots. On the left, the LiCAS robotic arms suspended by a drone for aerial manipulation tasks [8]; on the right, the CRANEbot system with two Pilz arms suspended by a crane for industrial tasks at CERN.

or, to account for all the possible deformation modes, via Cosserat rod theory [11,12]. When dealing with actuated loads instead, only approximate single or double pendulum models have been proposed and adopted so far [13,14]. However, these models prove inadequate in capturing the intricate dynamic effects that appear when the articulated suspended system is an actuated robotic manipulator, failing to account for the dynamic coupling between the two platforms. For these reasons, more comprehensive modelling approaches are required.

Moreover, the deployment of model-based control strategies is usually hindered by the absence of realistic simulation environments, which are helpful for their development, testing and sim-to-real transfer [15]. Indeed, existing rigid-body dynamic simulators (e.g., Gazebo [16]) do not offer the possibility of simulating cable-suspended robotic systems due to the difficulty of: (i) simulating deformable structures as infinite dimensional systems require approximate or finite elements models; (ii) handling constraints embedded in closed-chain structures created by the presence of multiple cables.

Motivated by this, here we propose modelling, identification, and simulation methods to tackle these open problems in cable-suspended dual-arm robotic manipulation. The two systems shown in Fig. 1 are considered as case studies to show and validate the generality of the proposed approach. The system on the left is an aerial cable-suspended dual-arm system used to install bird diverters on high-voltage power lines [2,8,17]. In that system, four belts, tied in a parallel pattern to a drone and a lower platform, hold two four-DoF (Degree of Freedom) LiCAS manipulators. The system on the right is the CRANEbot, a bimanual system designed by the European Organization for Nuclear Research (CERN) for inspecting and maintaining particle accelerator-related infrastructures [3,18]. In this case, a set of pulleys and steel ropes, coupled through a hook to a lower platform, serves as a lifting mechanism to hoist an articulated system (two Pilz© PRBT6 arms) from an overhead crane. In the following we show that the proposed modelling and identification methodology can handle the two cable configurations with minor modifications and can be easily extended to a wider variety of cable-suspended robotic systems.

The main contribution of this work can be thus summarised as follows:

- We propose a simplified open-chain rigid-body dynamic model of multi-cable-suspended robotic structures that can be readily integrated into standard physics-based robot simulators. This is the first work proposing such a modelling approach for this kind of robotic systems, up to the authors' knowledge.
- We developed a model identification procedure for such systems to reduce the sim-to-real gap when developing and deploying control methods for such systems (e.g., oscillations suppression techniques [19]). The proposed method overcomes the lack of one-to-one joints correspondence between the model and the real system maximising the similarity of their oscillatory behaviour. Moreover it takes into account constraints imposed by the presence of cables.
- We released the environment and the related source code to simulate cable-suspended dual-arm manipulators with the developed realistic models.

The rest of the paper is organised as follows: Section 2 provides an overview of the pertinent literature in the field; Section 3 discusses the system model while Section 4 its identification procedure; Section 5 encompasses the experiments conducted and their respective outcomes; Section 6 compares simulation with baseline modelling approaches, while Section 7 concludes the paper by discussing open challenges.

2. Related works

The focus of this section is to provide an overview of modelling and simulation methods for long-reach robotic systems featuring non-actuated, flexible cables.

As stated in the Introduction, long-reach features are generally provided to robots to access large but difficult-to-access workspaces. When the inspection site is accessible from above, it can be convenient to use robot manipulators suspended to an upper platform through one or multiple cables. This enlarges the robot workspace while also reducing dynamic coupling effects possibly caused by the interaction of the manipulator with hard environments [5,6,8]. This proves particularly useful in aerial systems, where articulated manipulators rigidly attached to a drone may not suffice to keep a safe distance between the rotors and the inspected areas [4,20,21], and where unavoidable impacts and overloads may destabilise the position control of the aerial platform [22]. Thus, inserting spring elements in the manipulator's joints and/or using flexible suspension cables can help alleviating these problems [23–25].

Although cable-suspended robotic systems proved to be inherently safe, the second-order pendulum dynamics resulting from the presence of non-actuated flexible elements may result in an oscillatory behaviour that needs to be accounted for. With the assumption of rigid bodies and inextensible cables, this dynamics can be mathematically captured by lumped mass models following three alternative baseline approaches [13,14,26]: (i) single pendulum, where the lower manipulation platform is thought of as a single suspended mass; (ii) double pendulum, where the first portion is represented by the hoisting cables and the second by the lower platform; and (iii) multi-cable models, used when the constraints imposed by the cable system cannot be approximated with those of a single one. The latter approach is more realistic but requires imposing holonomic constraints in the entire system dynamic model that accounts for the presence of the cables [27]. Although useful for controller design, the constrained model cannot be easily simulated through classical rigid-body dynamic engines. Moreover, none of the above-listed approaches is able to capture the dynamic coupling effects arising when the motion of the cable-suspended load is actuated, as in the examined case studies. Thus, modelling the entire structure using one of these methods is undoubtedly erroneous. The development of more accurate models may pave the way towards the development of model-based control techniques useful to e.g. reduce oscillations [13,28,29] exploiting the suspended manipulators' motion [30,31] and/or the actuation of the suspension platform [32].

Physics-based simulation provides an accelerated and safe avenue for developing, verifying, and testing robotic control algorithms and prototype design [15]. Robots are typically represented in simulation as a collection of rigid bodies connected through joints whose dynamics are computed via rigid-body algorithms [33]. This approach is unsuitable when the robot features flexible elements such as cables. As a matter of fact, researchers have started applying rigid-body dynamic modelling approaches also to flexible robots, such as soft robotic arms,

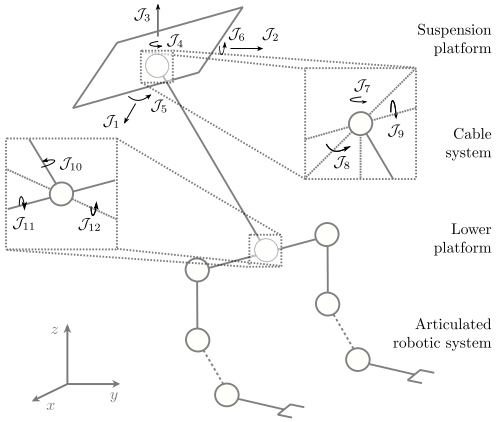

Fig. 2. The proposed generic kinematic model of dual-arm manipulator systems in cable-suspended pendulum configuration. $\mathcal{J}_i$ denotes the ith joint.

to exploit simulation and control architectures from the rigid-body literature [34,35]. This simplifies the process of testing control software in simulation and transferring it onto the physical system [36]. However, this requires the simulation to accurately emulate the real-world environment. To realise this, the robot model dynamics must be accurately identified via suitable identification procedures. To date, there is no published work about identification methods purposely designed for robots endowed with cables. As matter of fact, dynamic simulation of an aerial cable-suspended dual-arm manipulator can be achieved in this way only accepting a large sim-to-real gap [5].

3. System model

A cable-suspended robotic manipulation system can be built in many different ways. Therefore, deriving a general model of such a system requires a more in-depth analysis of its main components. Looking at Fig. 1, four key elements can be recognised: (*a*) an upper suspension platform, (*b*) a cable system, (*c*) a lower platform, and (*d*) one or more manipulators. The upper platform, which supports the entire system, can be a drone, an overhead crane, or the overall system can hang directly from the ceiling. Cables come in various shapes and sizes: for lifting systems, one can either utilise polyester straps or ropes made of a metal core (typically steel) wrapped in strands. Some possibilities for connecting the cables to (*a*) and (*c*) include winding them into pulleys, tying them with hook-and-loop joints, or knotting them at the ends. The payload is represented by (*c*) and (*d*), and their combination constitutes a robotic system with the lower platform acting as the manipulators' mechanical basis.

The conveyance of cable-suspended robotic systems necessitates precise control of the suspension platform, such as drones or cranes, which must operate at low speeds and avoid sudden changes in direction. Furthermore, this transportation process typically does not entail interactions with the surrounding environment. Consequently, it is reasonable to assume that the cable remains consistently taut and non-extensible in such circumstances. The proposed generic model of a cable-suspended robotic system, shown in Fig. 2, is described below and later customised for the particular systems considered in this paper. Since the real cable structure forms a closed kinematic chain, an equivalent open kinematic chain is adopted to simulate these systems using customary rigid-body dynamic software. The equivalence between the adopted open kinematic chain and the real system is later established by enforcing cable kinematic constraints and maximising the similarity of their dynamic response, as explained in the following.

Suspension platforms are assumed to have 6 DoFs, allowing unrestricted movement in three-dimensional space. Consequently, the motion of the suspension platform can be represented by a combination of three prismatic and three revolute joints, with each joint followed by a link representing the platform. The cables' motion can be represented by an additional 6 DoFs achieved by employing spherical joints at the interfaces with the upper and lower platforms. Three revolute joints with coincident origins and perpendicular axes are utilised to replace the upper spherical joint, followed by links that represent the cables. Similarly, the lower spherical joint is substituted by three revolute joints, where the subsequent link symbolises the lower platform. These 12 degrees of freedom (DoFs) can be appropriately coupled or virtually constrained/eliminated to align with the kinematics of the specific system. For instance, unless a fully actuated hexacopter is employed, multirotor attitude-translational coupling reduces the number of DoFs. Similarly, an overhead crane restricts its motion to a plane, resulting in only two translational DoFs. The manipulators, which typically consist of prismatic and/or revolute joints, already have known kinematics. Considering M as the number of joints in the manipulation system, the complete model of the cable-suspended system encompasses $N = 12 + M$ DoFs. It is important to note that joints $\mathcal{J}_1 \dots \mathcal{J}_6$ and $\mathcal{J}_{13} \dots \mathcal{J}_N$ are generally mechanically actuated (active), while joints $\mathcal{J}_7 \dots \mathcal{J}_{12}$, representing the cables, are non-actuated (passive).

Once the kinematics has been defined, its dynamic model can be deduced through the following equation

$$\boldsymbol{B}(\boldsymbol{q})\ddot{\boldsymbol{q}} + \boldsymbol{n}(\boldsymbol{q}, \dot{\boldsymbol{q}}) = \boldsymbol{u} - \boldsymbol{u}_e. \tag{1}$$

On the left side $\boldsymbol{q}(t)$, $\dot{\boldsymbol{q}}(t)$, $\ddot{\boldsymbol{q}}(t) \in \mathbb{R}^N$ are respectively the joints position, velocity, and acceleration vectors, $\boldsymbol{B}(\boldsymbol{q}) \in \mathbb{R}^{N\times N}$ is the inertia matrix, and $\boldsymbol{n}(\boldsymbol{q}, \dot{\boldsymbol{q}}) \in \mathbb{R}^N$ is the vector collecting centrifugal, Coriolis, and gravitational terms. On the right side, $\boldsymbol{u}(t) \in \mathbb{R}^N$ is the generalised joints actuation vector, while $\boldsymbol{u}_e(t) \in \mathbb{R}^N$ is the vector of the torques and forces at the joints induced by the interaction with the environment, defined as $\boldsymbol{u}_e(t) = \boldsymbol{J}(\boldsymbol{q})^T \boldsymbol{h}_e(t)$, where $\boldsymbol{J}(\boldsymbol{q}) \in \mathbb{R}^{N\times 6}$ is the Jacobian matrix and $\boldsymbol{h}_e(t) \in \mathbb{R}^6$ denotes the vector of forces and moments exerted by the manipulators' end-effectors on the environment.

Controlling the motion of a system means determining $\boldsymbol{u}(t)$ such that $\boldsymbol{q}(t) = \boldsymbol{q}^d(t)$ and $\dot{\boldsymbol{q}}(t) = \dot{\boldsymbol{q}}^d(t)$ where $\boldsymbol{q}^d(t) \in \mathbb{R}^N$ and $\dot{\boldsymbol{q}}^d(t) \in \mathbb{R}^N$ describe the desired trajectory. For our purposes, $\boldsymbol{u}(t)$ has been chosen as a set of proportional–derivative (PD) controllers, i.e.

$$\boldsymbol{u} = \boldsymbol{K}_d\dot{\tilde{\boldsymbol{q}}} + \boldsymbol{K}_p\tilde{\boldsymbol{q}}, \tag{2}$$

where $\dot{\tilde{\boldsymbol{q}}}(t) = \dot{\boldsymbol{q}}^d - \dot{\boldsymbol{q}}$ and $\tilde{\boldsymbol{q}}(t) = \boldsymbol{q}^d - \boldsymbol{q}$ are the velocity and position error, respectively, while $\boldsymbol{K}_p = \text{diag}\{k_{p,1}, \dots k_{p,n}\} \in \mathbb{R}^{N\times N}$ and $\boldsymbol{K}_d = \text{diag}\{k_{d,1}, \dots k_{d,n}\} \in \mathbb{R}^{N\times N}$ are semi positive-definite diagonal gain matrices with the physical interpretation of springs and dampers respectively, acting on the ith joint. This choice has a threefold motivation: (i) concerning active joints, robot manipulators are often equipped with position and velocity controllers, hence a feedback of those signal is always available; (ii) for the passive ones, although they are not actuated, they usually exhibit elastic and viscous friction behaviours, which can be replicated through such gains; (iii) it allows easy implementation of the virtual constraints to tie the generic model to the particular system, as shown in Section 5.2.

4. Model parameters identification

In the proposed open-chain rigid-body model described by Eqs. (1)–(2), each link is characterised by ten parameters, including mass, inertia tensor, and centre of mass position. Similarly, each joint is described by two parameters for friction (using the Coulomb-viscous model) and two parameters for proportional–derivative gains. To accurately represent a real cable-suspended system, the model requires knowledge of the parameter set $\boldsymbol{p} \in \mathbb{R}^P$ mentioned earlier. Parameters associated with rigid components, such as manipulators and platforms, are typically either already known or can be estimated using conventional identification methods (see e.g. [37,38]). These methods leverage the linearity property of the manipulator's dynamic model by utilising measurements of position, velocity, and torque, which are typically available

(or reconstructable) from the sensors on the manipulators actuation system. However, estimating parameters for non-rigid parts (cables) and passive joints is challenging because: (i) they lack of one-to-one correspondence in the real system since, as seen in Section 3, the cable suspension system is modelled as set of connected rigid-links through rotational joints with the same origin; (ii) passive joint measures (position, velocity, torque) are not available unlike their active counterpart; (iii) there is the need to capture the intricate kinematic and dynamic constraints imposed by the presence of cables. Consequently, classical identification approaches are unsuitable, necessitating the proposal of an alternative procedure.

The proposed technique allows the determination of the value of unknown model parameters utilising measurements obtained during the execution of oscillatory motions imposed on the system through manual changes to the initial state and through manipulator movements. With reference to Section 3, the values to be determined and referred to hereafter are therefore those related to the joints $\mathcal{J}_7 \dots \mathcal{J}_{12}$, and the corresponding virtual links and PD controllers. We assume that, during a set of experiments involving the generation of oscillations of the suspended system, a data recording mechanism (motion capture, fiducial markers, GPS, etc.) is used to determine the time series of poses of the lower platform in a given reference frame. The identification procedure consists in solving an optimisation problem to find the set of parameters $\hat{\boldsymbol{p}} \in \mathbb{R}^P$ to minimise the deviation between the actual recorded behaviour of the system, assessed through a number N_e of measured trajectories N_e measures, and the forward simulated model, maximising their similarity. The number $\boldsymbol{N_e}$ of acquired trajectories must be chosen beforehand, finding a compromise between the accuracy of the parameter identification procedure and its computational burden. We define this optimisation problem as follows

$$\begin{aligned} \hat{\boldsymbol{p}} = \arg\max_{\boldsymbol{p}} \ & \frac{1}{N_e} \sum_{i=1}^{N_e} R\left(\boldsymbol{x}_m^i, \boldsymbol{x}_s^i(\boldsymbol{p})\right) \\ \text{s.t.} \ & \underline{\boldsymbol{p}} \le \boldsymbol{p} \le \overline{\boldsymbol{p}} \,, \end{aligned} \tag{3}$$

where $\boldsymbol{x}_m^i = \{\boldsymbol{x}_m^i(0), \boldsymbol{x}_m^i(dt), \dots, \boldsymbol{x}_m^i(T)\}$ is the trajectory of the system's state recorded during the ith experiment (with dt and T denoting the time step and trajectory duration, respectively), $\boldsymbol{x}_s^i(\boldsymbol{p})$ denotes the corresponding trajectory signal obtained from the forward simulated model, while $R(\cdot)$ represents a metric of similarity between the two sets of signals. Lower and upper bound constraints, $\underline{\boldsymbol{p}}$ and $\overline{\boldsymbol{p}}$, are respectively necessary to guarantee the physical consistency of the optimisation result (e.g., the links' mass must always be positive, as well as the friction coefficients and the control gains) and to ensure a fast convergence while preventing unnecessary computational effort. Hereafter, the time dependence t and the apex i will be omitted for clarity. Vectors $\boldsymbol{x}_m$ and $\boldsymbol{x}_s$ embed measured/simulated state trajectory of the system, i.e., the pose trajectory of the lower platform in a three-dimensional space. The presence of cables restricts the set of poses the lower platform can assume, rendering its trajectories similar to those of a spherical pendulum. In particular For this reason, the data of interest are the x-y position r^x, r^y and orientation around the vertical axis ϕ^z of the platform with respect to its initial rest state, i.e., $\boldsymbol{x}_m = \begin{bmatrix} r_m^x & r_m^y & \phi_m^z \end{bmatrix}^T$ and $\boldsymbol{x}_s = \begin{bmatrix} r_s^x & r_s^y & \phi_s^z \end{bmatrix}^T$. At the kth instant of time, $\boldsymbol{x}_s(k)$ is a function of the system state (i.e., joints position and velocity vectors) that depends on the set $\boldsymbol{p}$ of the model dynamic parameters, according to $\boldsymbol{x}_s(k) = \boldsymbol{g}\left(\boldsymbol{q}(k, \boldsymbol{p})\right)$. More specifically, with L being the cables' length

$$\boldsymbol{g}\left(\boldsymbol{q}(k, \boldsymbol{p})\right) = \begin{bmatrix} L \sin q_8(k), & L \sin q_9(k), & q_7(k) + q_{10}(k) \end{bmatrix}^T . \tag{4}$$

A forward-Euler integration scheme is employed to derive $\boldsymbol{q}(k+1, \boldsymbol{p})$ from the direct dynamics of the system, i.e.,

$$\begin{aligned} \ddot{\boldsymbol{q}}(k, \boldsymbol{p}) = & \boldsymbol{B}\left(\boldsymbol{q}(k)\right)^{-1} \Big[\boldsymbol{K}_d \dot{\tilde{\boldsymbol{q}}}(k) + \boldsymbol{K}_p \tilde{\boldsymbol{q}}(k) \\ & - \boldsymbol{n}\left(\boldsymbol{q}(k), \dot{\boldsymbol{q}}(k)\right) - \boldsymbol{J}^T\left(\boldsymbol{q}(k)\right) \boldsymbol{h}_e(k) \Big] . \end{aligned} \tag{5}$$

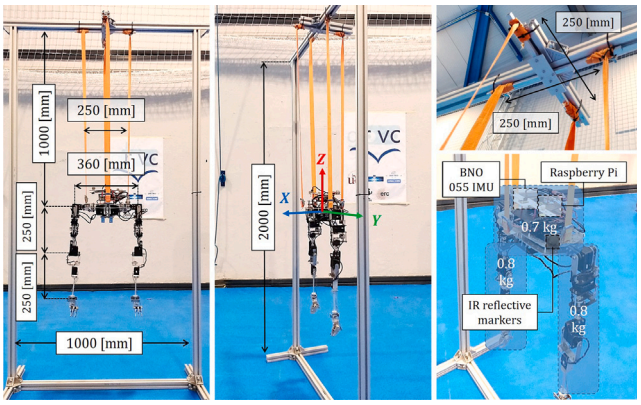

Fig. 3. Setup of the LiCAS A1 in 4-cable-suspended configuration.

Integrating equation (5) and using Eq. (4) the symbolic trajectory $\boldsymbol{x}_s(\boldsymbol{p})$ can be constructed as function of the unknown parameters $\boldsymbol{p}$ to be then used in Eq. (3). When evaluated numerically, the model initial conditions $\boldsymbol{q}_0$ and $\dot{\boldsymbol{q}}_0$ have to be set consistently with the state of the physical system at the beginning of the experiments. Similarly, it is essential that $\boldsymbol{q}^d$ and $\dot{\boldsymbol{q}}^d$ align with the real trajectories applied to the manipulators to induce the oscillatory movements.

At this point, our objective is to maximise the similarity between the real measured signals $\boldsymbol{x}_m$ and the output of the model. To this end, a metric of similarity must be chosen. A metric of similarity numerically quantifies how closely related data samples are. Values range between zero (indicating low similarity or dissimilarity) and one (indicating high similarity or likeness). Regarding the metric for signals similarity in the definition of the cost function of Eq. (3), the Pearson product-moment cross-correlation coefficient has been employed. Cross-correlation provides indeed information on the similarity between two different time series and the Pearson correlation coefficient is its normalised version. The Pearson cross-correlation is a metric that measures the linear relationship between two time-series while considering both amplitude and time shifts. It is a variant of the more general cross-correlation metric. It is beneficial when examining the similarity between two signals while accounting for potential time lags. Given two sampled time-series signals $x(t)$ and $y(t)$, the coefficient $\rho(x, y)$ is defined as

$$\rho(x, y) = \frac{1}{N-1} \sum_{k=1}^{N} \left(\frac{x(k) - \mu_x}{\sigma_x} \right) \left(\frac{y(k) - \mu_y}{\sigma_y} \right) \tag{6}$$

where N is the number of samples, μ_x and σ_x are the mean and standard deviation of x, and μ_y and σ_y are the mean and standard deviation of y. The possible range for ρ is $[-1, 1]$, the closer the value is to 1, the more closely the sets of signals are identical. Vectors $\boldsymbol{x}_m$ and $\boldsymbol{x}_s$ typically contain multiple signals. Each element of the vector is then compared independently, and the mean correlation value is computed, i.e.,

$$R(\boldsymbol{x}_m, \boldsymbol{x}_s) = \frac{1}{3} \left[\rho(r_m^x, r_s^x) + \rho(r_m^y, r_s^y) + \rho(\phi_m^z, \phi_s^z) \right]. \tag{7}$$

Finally, regarding the parameters to be identified, the procedure involves inputting the known links parameters (articulated robotic system and lower platform) into the model and allowing the optimisation process to yield the parameters pertaining to the cable-representative links as well as the values of friction and gains of the PD virtual controllers on joints $\mathcal{J}_7 \dots \mathcal{J}_{12}$.

5. Experimental setup and validation results

As explained in Section 4, parameter estimation (*identification*) entails the utilisation of one or more experiments. Once an estimate is obtained, the parameters are substituted into the model, and the

behaviour of the simulated system is compared with a fresh set of experiments (*validation*). This section describes the two experimental setups used to retrieve the measurement data (Section 5.1), the necessary customisation of the generic model of Eq. (1) and (2) for each of the systems (Section 5.2), and the identification procedure validation (Section 5.3).

5.1. Experimental setup

The modelling and identification methods described previously have been tested on the two long-reach dual-arm robotic platforms shown in Fig. 1.

The first platform is a lightweight and compliant anthropomorphic dual-arm system (LiCAS) in a 4-Cable Suspended configuration, shown in Fig. 3. The human-size and human-like arms employ Herkulex DRS-0402/0602 smart servos assembled in a customised frame manufactured in aluminium and carbon fibre. Four harnesses support the arms' shoulder structure (0.7 kg weight) by 1 m long / 250 mm separated cables, as depicted in Fig. 3. The arms are fed by a 3 S 1600 mAh LiPo battery and controlled through a C/C++ program executed on a Raspberry Pi Model 3 connected to the WiFi network of the OptiTrack™testbed to log the positioning data and the data from the BNO 055 inertial measurement unit (IMU) also integrated into the shoulder structure.

The second platform, the CRANEbot, is lifted by overhead cranes, which allows operations to be carried out from above, performing remote procedures in radioactive areas at CERN that cannot be reached by ordinary ground robots. The load (190 kg), lifted through to the overhead crane lifting system at the height of 3.897 m via a crane hook adapter, is equipped with an on-board camera system and two six-axis Pilz© PRBT 6 manipulator arms mounted at a horizontal distance of 380 mm, controlled through a C++ framework executed on an Intel® on-board computer and powered by 8 Lead-gel 13000 mAh rechargeable batteries, arranged in the central body together with modules for WiFi/4G connection. The lower platform was equipped with a set of ArUco markers for the experiments, whose pose was detected through external Axis® PTZ high-resolution IP cameras.

To capture the cable system dynamics and its coupling with the actuated load, in the following, the suspension platforms are left out of the model and will be included in future work. For this reason, the drone for LiCAS has been directly substituted by a testbed, and the crane for CRANEBot is kept stationary in its initial configuration. In order to excite the oscillatory dynamics of the systems, two types of experiments were conducted: *unforced* oscillations (Section 5.3.1) and *arms-induced* oscillations (Section 5.3.2). In the first case, an operator manually modifies the lower platform's starting position causing a displacement from its rest state (see Fig. 4), while in the second, the arms move following a trajectory which is a sum of cubic polynomials so as to generate oscillations of the suspension structure. Motion tracking systems record the pose of the lower platforms during the generated oscillatory behaviour.

5.2. Customisation of the dynamic model

The generic model expressed by Eq. (1) and (2) has been customised for the two addressed case studies. The LiCAS system results in $M=8$ (two 4-DoFs manipulators) and $N=20$. Since the testbed is stationary, the first six joints do not enter into the model. LiCAS exhibits some notable behaviours: (*i*) if the lower platform rotates around the vertical axis, it returns to its initial configuration according to a damped elastic behaviour (see Fig. 5(b)); (*ii*) the parallel arrangement of the four cables ensures the lower platform to stay always parallel to the ground (see Fig. 5(a)). For the elastic return to the vertical rest position, two PD controllers as in Eq. (2) have been adopted for $\mathcal{J}_7$ and $\mathcal{J}_{10}$, i.e., $k_{d,7}$, $k_{p,7}$, $k_{d,10}$, $k_{d,10} \neq 0$ and q_7^d, $\dot{q}_7^d$, q_{10}^d, $\dot{q}_{10}^d = 0$. Two PD controllers on $\mathcal{J}_{11}$ and $\mathcal{J}_{12}$ are inserted to model the horizontal behaviour of the lower platform. From geometrical considerations, it is easy to understand that the platform stays parallel to the ground if $\mathcal{J}_{11}$ and $\mathcal{J}_{12}$ have the same and opposite motion as $\mathcal{J}_8$ and $\mathcal{J}_9$ respectively, as a consequence $k_{d,11}$, $k_{d,12}$, $k_{p,11}$, $k_{p,12} \neq 0$ and $q_{11}^d = q_8$, $\dot{q}_{11}^d = \dot{q}_8$, $q_{12}^d = q_9$ and $\dot{q}_{12}^d = \dot{q}_9$.

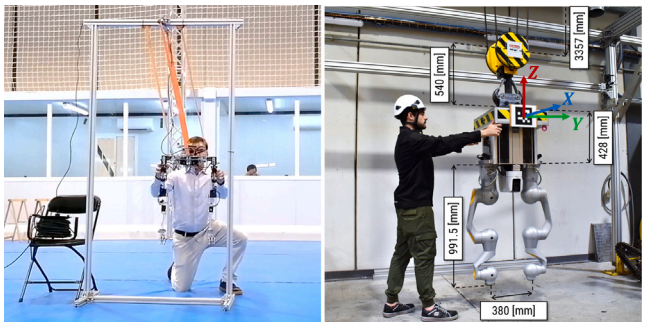

Fig. 4. Experimental setup for the identification measurements: manual modification of the starting condition for LiCAS (left) and CRANEbot (right).

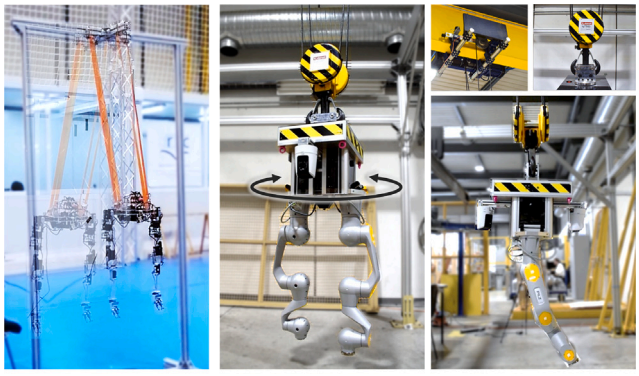

(a) (b) (c)

Fig. 5. (a) Lower platform stays parallel to the ground along a lateral displacement; (b) Rotation about the vertical axis of the lower platform, before elastically returning to its rest position; (c) Detail of the suspension system and mechanical block of the hook's rotation with respect to the pulleys during a lateral movement of the arms.

For CRANEbot instead, $M=12$ (two 6-DoFs manipulators) and $N=24$. Again, since the crane is stationary, the first six DoFs do not enter the model. This system exhibits the following remarkable behaviours: (*i*) as before a damped elastic behaviour occurs when the lower platform rotates around the vertical axis; (*ii*) the coupling between the pulley and hook blocks any tilting movement of the lower platform (see Fig. 5(c)), which remains mechanically paired to the cables system. For the elastic return to the vertical rest position, the same approach of using PD controllers for $\mathcal{J}_7$ and $\mathcal{J}_{10}$ applies. Rotation about the lower platform can instead be virtually blocked by inserting PD controllers as in Eq. (2) on $\mathcal{J}_{11}$ and $\mathcal{J}_{12}$, commanding the joints to track their zero position, i.e., $k_{d,11}$, $k_{p,11}$, $k_{d,12}$, $k_{p,12} \neq 0$, and q_{11}^d, q_{12}^d, $\dot{q}_{11}^d$, $\dot{q}_{12}^d = 0$.

5.3. Identification and validation results

The entire implementation of the identification framework has been executed in MATLAB®. A nonlinear programming solver (*fmincon*) has been adopted for the optimisation. Among the available minimisation algorithms, the *active-set* was chosen to facilitate more substantial steps, enhancing convergence speed compared to the alternatives. The code was executed using the Parallel Computing Toolbox™to expedite the computations. The integration step for the model was set to 1 ms. The outcomes deriving from unforced oscillation for LiCAS and arms-induced for CRANEbot will be shown. The following experimental

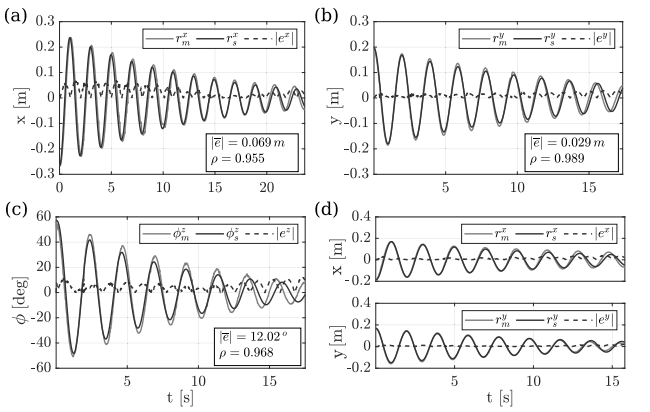

Fig. 6. Comparison between simulated model (grey line) and validation signals (black line) with unforced oscillations: (a)–(c) involve a modification of the position along x, y and z axes respectively while (d) involves a combined motion along the x and y axes. The dotted line shows the error between simulation and real data. Pearson cross-correlation coefficient ρ and maximum error $|\overline{e}|$ values are shown in the bottom right box.

results focus on main axis motions, but due to system nonlinearity, unforced or arms-induced oscillations involve all axes. The measures include oscillations along all axes for identification and validation despite the main axis emphasis.

5.3.1. Unforced oscillations

In these experiments, an operator manually adjusts the robot's initial pose by pulling the lower platform (see Fig. 4). To perform LiCAS identification, three measurement pairs were employed. Each pair involves a modification of a single component that determines the initial configuration of the platform, precisely the position along x-axis (r^x), the position along y-axis (r^y), and the orientation around z-axis (ϕ^z), as illustrated in Fig. 3. Additionally, the validation process encompasses four additional measurements. Three of these measurements follow the configuration above, while the last involves a combined motion along the x and y axes. Because of the removal of the suspension platform, the subsequent discussion will focus on the remaining joints. First, it will address the dynamic parameters featured in Eq. (1). Then, the controller gains as outlined in Eq. (2). Concerning the dynamic parameters, the ones related to the manipulators and the lower platform, i.e., masses ($m_{10} \dots m_{20}$), centres of mass ($\boldsymbol{l}_{10} \dots \boldsymbol{l}_{20}$), inertia tensors ($\boldsymbol{I}_{10} \dots \boldsymbol{I}_{20}$), and friction coefficients ($f_{v,10} \dots f_{v,20}$) are known and can be directly substituted into the model. The ones instead related to cables ($m_7 \dots m_9$, $\boldsymbol{l}_7 \dots \boldsymbol{l}_9$, $\boldsymbol{I}_7 \dots \boldsymbol{I}_9$, and $f_{v,7} \dots f_{v,9}$) are unknown and need to be identified. Note that m_7 and $\boldsymbol{l}_7$ do not enter into the model since they are irrelevant to the rotational dynamics around joint $\mathcal{J}_7$. Finally, it was assumed that the centres of mass of the cable links have components solely along the cables' vertical axis, i.e., $\boldsymbol{l}_i = \begin{bmatrix} 0 & 0 & l_i^z \end{bmatrix}^T$ with $i = 8, 9$, and that their inertia tensors $\boldsymbol{I}_7, \boldsymbol{I}_8, \boldsymbol{I}_9$ are all diagonal matrices in the form $\text{diag}\{i_{xx}, i_{yy}, i_{zz}\}$. Regarding the controller gains in Eq. (2), the values for manipulator controllers, i.e., joints $\mathcal{J}_{13} \dots \mathcal{J}_{20}$, are known and can be directly substituted. Joints $\mathcal{J}_8$ and $\mathcal{J}_9$ do not show any peculiar behaviour, so their gains are null. On the other hand, joints $\mathcal{J}_7, \mathcal{J}_{10}, \mathcal{J}_{11}, \mathcal{J}_{12}$ exhibit peculiar behaviours modelled through PD controllers, so their values need to be identified.

Table 5 shows the list of parameters $\boldsymbol{p}$ included in the identification process, together with their initial value $\boldsymbol{p}_0$ (starting point of the optimisation algorithm), the upper bound $\overline{\boldsymbol{p}}$, and the estimate $\hat{\boldsymbol{p}}$. The lower bound $\underline{\boldsymbol{p}}$ values were all set to zero for physical consistency. At the end of the identification process, the cost function yields a total value of 0.9715. Fig. 6 compares the validation measurements and the signals obtained from the simulation after incorporating the estimated parameters into the model. Every graph within the analysis

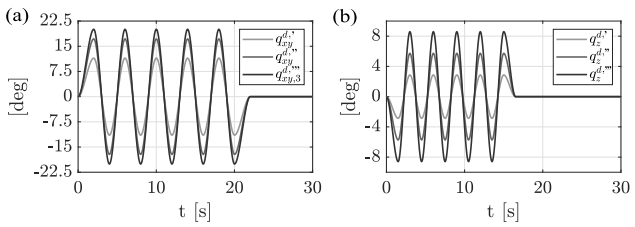

Fig. 7. (a) Sinusoidal joints reference q^d_{xy} for the generation of three oscillations of different amplitudes around x and y axes. The joint reference maximum amplitude has been set to 11.5 deg for the first trajectory $q^{d'}_{xy}$, to 17 deg for $q^{d''}_{xy}$ and to 20 deg for $q^{d'''}_{xy}$. (b) Sinusoidal joints reference q^d_z for the generation of three oscillations of different amplitudes around z axis. The joint reference maximum amplitude has been set to 2.85 deg for the first trajectory $q^{d'}_z$, to 5.7 deg for $q^{d''}_z$ and to 8.6 deg for $q^{d'''}_z$.

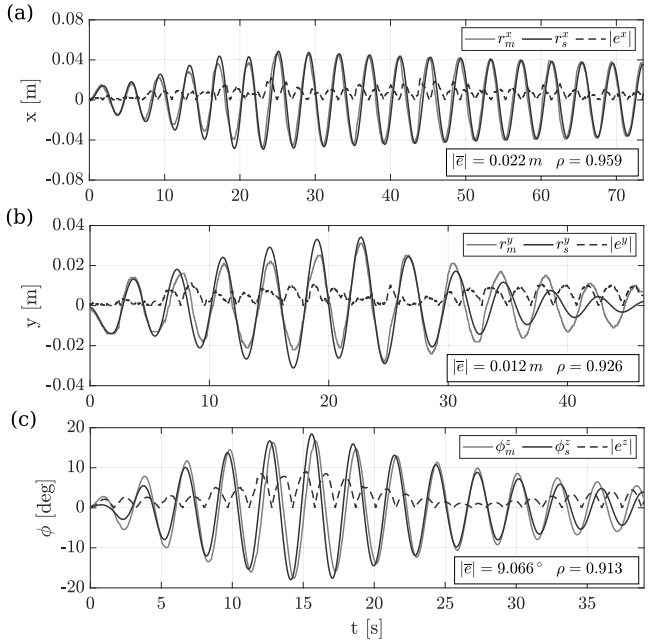

Fig. 8. Comparison between simulated model (grey line) and validation signals (black line) with arms-induced oscillations: (a)–(c) involve a modification of the position along x, y and z axes respectively. The dotted line shows the error between simulation and real data. Pearson cross-correlation coefficient ρ and maximum error $|\overline{e}|$ values are shown in the bottom right box.

Table 1
MAE and MRE for LiCAS identification.

	exp X	exp Y	exp Z	exp XY
Abs err	0.0204 m	0.0126 m	4.867°	0.013 m / 0.010 m
Rel err %	27.08	18.45	15.89	16.04 / 16.25

showcases the Pearson cross-correlation coefficient ρ that quantifies the similarity between the measurement and simulation data, along with the absolute maximum error value $|\overline{e}|$ between the respective signals. Specifically, the correlation values obtained are 95.5%, 98.9%, and 96.8% for the first three experiments, while the x and y positions in the final experiment exhibit correlations of 98.5% and 99.4% respectively, accompanied by errors of $|\overline{e}^x| = 0.039$ m and $|\overline{e}^y| = 0.023$ m. Finally, the corresponding Mean Absolute Error (MAE) and Mean Relative Errors (MRE) are reported in Table 1.

Table 2
MAE and MRE for CRANEBot identification.

	exp X	exp Y	exp Z
Abs err	0.0072 m	0.0046 m	2.610°
Rel err %	31.8	42.71	39.3

5.3.2. Arms-induced oscillations

In these experiments, oscillations are induced by the movements of the arms. For the identification of the CRANEbot parameters, three pairs of measurement were utilised, with each pair corresponding to one of the axes shown in Fig. 4. Furthermore, three additional experiments, one for each axis, were conducted for validation. To excite cable-suspended oscillations, sinusoidal trajectories (see Fig. 7) were commanded to the second and third Pilz manipulator joints, with varying amplitudes and a frequency matching the system's resonance frequency. Specifically, the x and y axes were driven at a frequency of 0.25 Hz, while the z-axis oscillated at 0.33 Hz. Fig. 7 shows the joint's sinusoidal reference trajectories employed for the aforementioned experiments. Each experiment has been performed by modifying the amplitude of the commanded trajectory.

Similar considerations and assumptions can be made for the identification of this cable-suspended robot. The crane is fixed, and its joint dynamics do not enter the model. The parameters of the manipulators and the lower platform are known, cable centres of mass lie solely along the vertical axis, and inertia tensors have a diagonal form. Gains to be identified are only those related to the peculiar behaviours affecting the movement of the lower platform and the damped-elastic rotation around the vertical. Details on the configuration of the optimisation problem and the identified parameters $\hat{\boldsymbol{p}}$ can be found in Table 5. The cost function after the identification process for CRANEbot is 0.9472. Fig. 8 presents a visual comparison between the three pairs of measurements utilised for validation and the corresponding simulation data, after incorporating the estimated parameters into the model. The images exhibit a notable conformity of the oscillatory signals, showcasing that the movement of the arms elicits a simulated response that closely mirrors that of the physical system. This observation underscores the successful identification process, affirming that the simulated behaviour accurately captures the dynamic response of the actual system. In particular, for the validation, the correlation values x and y axes are 95.9% and 92.6% respectively, with maximum errors in the order some centimetres ($|\vec{e}^x| = 0.022$ m and $|\vec{e}^y| = 0.012$ m), while for the z-axis the correlation is 91.3% with a maximum error $|\vec{e}^z| = 9.066°$. Again, the corresponding Mean Absolute Error (MAE) and Mean Relative Errors (MRE) are reported in Table 2.

6. Simulation

Simulation can provide an amenable venue to preliminary test control strategies, which must rely upon the manipulation system or oscillation suppression control. Therefore, once the model customisation and identification are complete, the obtained parameters can be directly replaced in the simulator. The results in Section 4 hold valuable significance as they enable the simulation of a model that faithfully reproduces the behaviour of the real-world system by reducing the sim-to-real gap.

To build the simulation model shown in Figs. 9 and 10, we employed an open kinematic chain with 6 revolute joints to represent the cable structure as explained in Section 3. The model is described in URDF format and is endowed with a Gazebo model plugin that realises the dynamic behaviour resulting from the unilateral constraints imposed by cables. As a result, the lower platform can displace maintaining the horizontal configuration and exhibit an elastic behaviour around the vertical axis. The identification procedure illustrated in Section 4 leads to physically consistent dynamic parameters as used in this model. The equivalence of exhibited dynamic behaviour between the real and the simulated systems can be better appreciated in the video accompanying this paper, both in the case of unforced and arm-induced oscillations.

A comparison between our proposed model in Section 3 and two baseline pendulum models has been performed as supplementary evidence supporting the proposed approach. Fig. 11 shows the error on the LiCAS lower platform pose between a Gazebo simulation of an unforced oscillation experiment on y-axis and (i) a single pendulum model (ii) a double pendulum model (iii) the proposed model endowed with identified parameters. The employment of model (iii) ensured a maximum error reduction of respectively 64.4% and 85.9% when compared to (i) and (ii). Fig. 12 compares a CRANEbot simulation by making it start from a non-rest state and simultaneously moving the arms. The baseline models clearly cannot capture the dynamic coupling due to the movement of the arms, which is instead taken

Table 3
LiCAS arms: Inertia tensors.

	i_{xx}	i_{xy}	i_{xz}	i_{yy}	i_{yz}	i_{zz}
$\boldsymbol{I}_{10} \dots \boldsymbol{I}_{12}$	3.02e−3	0	0	8.64e−4	0	3.39e−3
$\boldsymbol{I}_{13}, \boldsymbol{I}_{14}$	3.53e−2	0	0	3.01e−2	9.04e−3	1.87e−2
$\boldsymbol{I}_{15}, \boldsymbol{I}_{16}$	3.58e−2	0	0	3.22e−3	−1.45e−3	3.66e−2
$\boldsymbol{I}_{17}, \boldsymbol{I}_{18}$	2.06e−2	0	0	1.08e−2	−5.36e−3	1.63e−2
$\boldsymbol{I}_{19}, \boldsymbol{I}_{20}$	6.79e−3	0	0	4.91e−3	2.67e−3	3.40e−3

Table 4
CRANEBot arms: Inertia tensors.

	i_{xx}	i_{xy}	i_{xz}	i_{yy}	i_{yz}	i_{zz}
$\boldsymbol{I}_{13}, \boldsymbol{I}_{14}$	3.53e−2	0	0	3.01e−2	9.04e−3	1.87e−2
$\boldsymbol{I}_{15}, \boldsymbol{I}_{16}$	3.58e−2	0	0	3.22e−3	−1.45e−3	3.66e−2
$\boldsymbol{I}_{17}, \boldsymbol{I}_{18}$	2.06e−2	0	0	1.08e−2	−5.36e−3	1.63e−2
$\boldsymbol{I}_{19}, \boldsymbol{I}_{20}$	6.79e−3	0	0	4.91e−3	2.67e−3	3.40e−3
$\boldsymbol{I}_{21}, \boldsymbol{I}_{22}$	7.37e−3	0	0	5.87e−3	−1.71e−3	3.96e−3
$\boldsymbol{I}_{23}, \boldsymbol{I}_{24}$	0	0	0	0	0	0

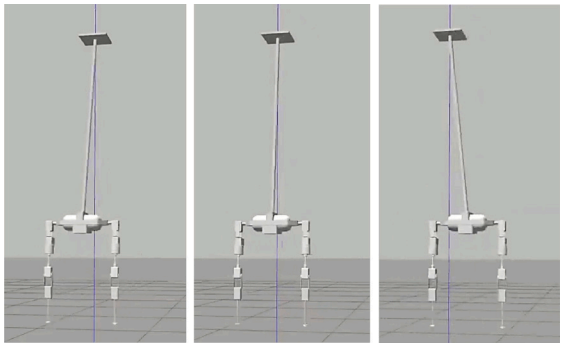

Fig. 9. Simulation in Gazebo of LiCAS while performing unforced oscillation.

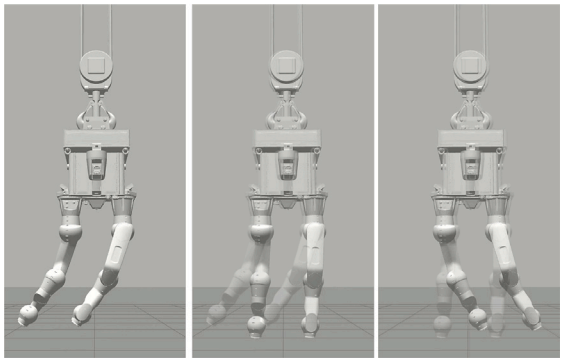

Fig. 10. Simulation in Gazebo of CRANEbot while performing an arms-induced oscillation.

Table 5
Dynamic model parameters[a].

p	Description	LiCAS			CRANEBot		
		p_0	$\overline{p}$	$\hat{p}$	p_0	$\overline{p}$	$\hat{p}$
$m_1 \dots m_6$	Mass links 1 … 6		Drone left out from the model			Crane left out from the model	
m_7	Mass link 7		Does not enter into the model			Does not enter into the model	
m_8 (⋆)	Mass link 8	1.0	10.0	4.237	30.0	45.0	35.55
m_9 (⋆)	Mass link 9	1.0	10.0	5.032	30.0	45.0	35.55
$m_{10} \dots m_{12}$	Mass lower platform	×	×	0.639	×	×	156.25
m_{13}, m_{14}	Mass arm first link	×	×	0.233	×	×	7.1
m_{15}, m_{16}	Mass arm second link	×	×	0.246	×	×	1.7
m_{17}, m_{18}	Mass arm third link	×	×	0.214	×	×	4.8
m_{19}, m_{20}	Mass arm fourth link	×	×	0.106	×	×	0.9
m_{21}, m_{22}	Mass arm fifth link	×	×	×	×	×	2.6
m_{23}, m_{24}	Mass arm sixth link	×	×	×	×	×	0.2
$\boldsymbol{l}_1 \dots \boldsymbol{l}_6$	CoM vectors links 1 … 6		Drone left out from the model			Crane left out from the model	
$\boldsymbol{l}_7$	CoM vector link 7		Does not enter into the model			Does not enter into the model	
l_8^z (⋆)	CoM link 8: $[0\ 0\ -l_8^z]$	0.1	1.0	0.174	0.1	3.5	1.894
l_9^z (⋆)	CoM link 9: $[0\ 0\ -l_9^z]$	0.1	1.0	0.824	0.1	3.5	1.894
$\boldsymbol{l}_{10} \dots \boldsymbol{l}_{12}$	CoM lower platform	×	×	[0, 0, 0]	×	×	[0, 0, −0.521]
$\boldsymbol{l}_{13}$, $\boldsymbol{l}_{14}$	CoM arm first link	×	×	[0, 0.0236, −0.00946]	×	×	[0, 0.026, 0.051]
$\boldsymbol{l}_{15}$, $\boldsymbol{l}_{16}$	CoM arm second link	×	×	[0, 0.04, 0]	×	×	[0, 0.162, −0.134]
$\boldsymbol{l}_{17}$, $\boldsymbol{l}_{18}$	CoM arm third link	×	×	[−0.015, 0, −0.1]	×	×	[0, 0.043, −0.027]
$\boldsymbol{l}_{19}$, $\boldsymbol{l}_{20}$	CoM arm fourth link	×	×	[0, 0, −0.143]	×	×	[0, 0.061, −0.204]
$\boldsymbol{l}_{21}$, $\boldsymbol{l}_{22}$	CoM arm fifth link	×	×	×	×	×	[0, 0.021, −0.032]
$\boldsymbol{l}_{23}$, $\boldsymbol{l}_{24}$	CoM arm sixth link	×	×	×	×	×	[0, 0, 0]
$\boldsymbol{I}_1 \dots \boldsymbol{I}_6$	Inertia tensors 1 … 6		Drone left out from the model			Crane left out from the model	
i_{xx} (⋆)	Inertia links 7 … 9 (xx)	0.0	2.0	0.313	0.0	100.0	35.37
i_{yy} (⋆)	Inertia links 7 … 9 (yy)	0.0	2.0	0.363	0.0	100.0	58.23
i_{zz} (⋆)	Inertia links 7 … 9 (zz)	0.8	5.0	0.745	0.0	100.0	5.807
$\boldsymbol{I}_{10} \dots \boldsymbol{I}_{12}$	Inertia lower platform		Values presented in Table 3			Values presented in Table 4	
$\boldsymbol{I}_{13}$, $\boldsymbol{I}_{14}$	Inertia arm first link		Values presented in Table 3			Values presented in Table 4	
$\boldsymbol{I}_{15}$, $\boldsymbol{I}_{16}$	Inertia arm second link		Values presented in Table 3			Values presented in Table 4	
$\boldsymbol{I}_{17}$, $\boldsymbol{I}_{18}$	Inertia arm third link		Values presented in Table 3			Values presented in Table 4	
$\boldsymbol{I}_{19}$, $\boldsymbol{I}_{20}$	Inertia arm fourth link		Values presented in Table 3			Values presented in Table 4	
$\boldsymbol{I}_{21}$, $\boldsymbol{I}_{22}$	Inertia arm fifth link	×	×	×		Values presented in Table 4	
$\boldsymbol{I}_{23}$, $\boldsymbol{I}_{24}$	Inertia arm sixth link	×	×	×		Values presented in Table 4	
$f_{v,7}$ (⋆)	Viscous friction $\mathcal{J}_7$	0.2	2.0	0.517	0.2	2.0	0.9
$f_{v,8}$ (⋆)	Viscous friction $\mathcal{J}_8$	0.1	3.0	1.33	1.0	600.0	485.3
$f_{v,9}$ (⋆)	Viscous friction $\mathcal{J}_9$	0.1	3.0	1.311	50.0	100.0	52.7
$f_{s,7}$ (⋆)	Static friction $\mathcal{J}_7$	0.0	1.0	0.0	0.0	1.0	0.01
$f_{s,8}$ (⋆)	Static friction $\mathcal{J}_8$	0.0	1.0	0.0	0.0	1.0	0.767
$f_{s,9}$ (⋆)	Static friction $\mathcal{J}_9$	0.0	1.0	0.0	0.0	1.0	0.0
$k_{d,7}$ (⋆)	D gain virtual controller $\mathcal{J}_7$	1.0	5.0	0.0	1.0	5.0	0.0
$k_{p,7}$ (⋆)	P gain virtual controller $\mathcal{J}_7$	15.0	50.0	17.86	40.0	50.0	30.92
$k_{d,10}$ (⋆)	D gain virtual controller $\mathcal{J}_{10}$	1.0	5.0	0.556	1.0	5.0	0.0
$k_{p,10}$ (⋆)	P gain virtual controller $\mathcal{J}_{10}$	10.0	50.0	0.021	1.0	50.0	0.041
$k_{d,11}$ (⋆)	D gain virtual controller $\mathcal{J}_{11}$	1.0	5.0	0.01	1.0	5.0	0.0
$k_{p,11}$ (⋆)	P gain virtual controller $\mathcal{J}_{11}$	100.0	1000	682.4	100.0	1000	953.2
$k_{d,12}$ (⋆)	D gain virtual controller $\mathcal{J}_{12}$	1.0	5.0	0.01	1.0	5.0	0.0
$k_{p,12}$ (⋆)	P gain virtual controller $\mathcal{J}_{12}$	100.0	1000	712.3	100.0	1000	891.5

[a] Values are presented in the following units: masses (kg), centres of mass (m), inertias ($\mathrm{kg\,m^2}$).
(⋆) Parameters identified.

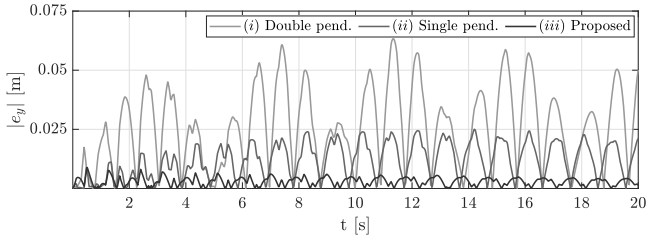

Fig. 11. Simulation in Gazebo of an arms-induced oscillation for LiCAS. Error between simulation data and (*i*) double pendulum model, (*ii*) single pendulum model, (*iii*) proposed model.

into account in the proposed model. This last reduces the maximum error of respectively 80.4% and 84.3% compared to single and double pendulum modelling approaches.

The environment and the related source code to simulate cable-suspended dual-arm manipulators are free at https://github.com/prisma-lab/cable-suspended-robots.

7. Conclusion

This paper proposed a rigid-body model of cable-suspended dual-arm robotic manipulators in a pendulum configuration. A dynamic parameters identification procedure was devised for the presented model to reduce the sim-to-real gap. Two cable-suspended dual-arm manipulation systems were used to assess the capability of the proposed model in handling different cable configurations and suspension mechanisms.

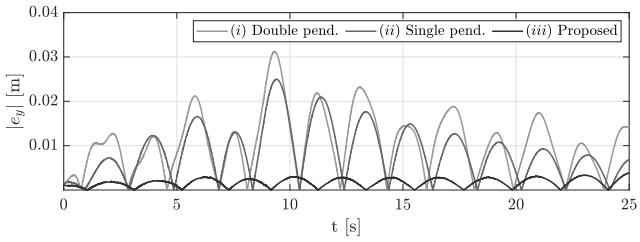

Fig. 12. Simulation in Gazebo of an arms-induced oscillation for CRANEbot. Error between simulation data and (*i*) double pendulum model, (*ii*) single pendulum model, (*iii*) proposed model.

The simulated and real response signals showed a high (from 91.3% to 99.4%) correlation, while the comparison between the proposed model and baseline pendulum modelling approaches shows a significantly increased simulation accuracy (from 64.4% to 85.9%). The proposed approach allows building realistic simulation environments useful for controller design, testing, and training of machine learning methods which are promising future works on the topic.

CRediT authorship contribution statement

Giancarlo D'Ago: Conceptualization, Data curation, Formal analysis, Investigation, Methodology, Resources, Software, Validation, Visualization, Writing – original draft, Writing – review & editing. **Mario Selvaggio:** Conceptualization, Investigation, Supervision, Writing – review & editing. **Alejandro Suarez:** Resources, Supervision. **Francisco Javier Gañán:** Data curation. **Luca Rosario Buonocore:** Project administration, Supervision. **Mario Di Castro:** Funding acquisition, Supervision. **Vincenzo Lippiello:** Funding acquisition, Supervision. **Anibal Ollero:** Funding acquisition. **Fabio Ruggiero:** Conceptualization, Investigation, Project administration, Supervision, Writing – original draft, Writing – review & editing.

Declaration of competing interest

The authors declare that they have no known competing financial interests or personal relationships that could have appeared to influence the work reported in this paper.

Data availability

Shared in the github repository linked in the manuscript.

Appendix A. Supplementary data

Supplementary material related to this article can be found online at https://doi.org/10.1016/j.robot.2024.104643.

References

[1] F. Ruggiero, V. Lippiello, A. Ollero, Aerial manipulation: A literature review, IEEE Robot. Autom. Lett. 3 (3) (2018) 1957–1964.
[2] A. Ollero, G. Heredia, A. Franchi, G. Antonelli, K. Kondak, A. Sanfeliu, A. Viguria, J.R. Martinez-de Dios, F. Pierri, J. Cortés, et al., The aeroarms project: Aerial robots with advanced manipulation capabilities for inspection and maintenance, IEEE Robot. Autom. Mag. 25 (4) (2018) 12–23.
[3] M. Di Castro, M. Ferre, A. Masi, CERNTAURO: A modular architecture for robotic inspection and telemanipulation in harsh and semi-structured environments, IEEE Access 6 (2018) 37506–37522.
[4] A. Suarez, P. Sanchez-Cuevas, M. Fernandez, M. Perez, G. Heredia, A. Ollero, Lightweight and compliant long reach aerial manipulator for inspection operations, in: 2018 International Conference on Intelligent Robots and Systems, 2018, pp. 6746–6752.
[5] A. Suarez, F. Real, V.M. Vega, G. Heredia, A. Rodriguez-Castaño, A. Ollero, Compliant bimanual aerial manipulation: Standard and long reach configurations, IEEE Access 8 (2020) 88844–88865.
[6] A. Suarez, R. Salmoral, P.J. Zarco-Periñan, A. Ollero, Experimental evaluation of aerial manipulation robot in contact with 15 kV power line: Shielded and long reach configurations, IEEE Access 9 (2021) 94573–94585.
[7] Y.S. Sarkisov, M.J. Kim, D. Bicego, D. Tsetserukou, C. Ott, A. Franchi, K. Kondak, Development of SAM: Cable-suspended aerial manipulator, in: IEEE International Conference on Robotics and Automation, 2019, pp. 5323–5329.
[8] I. Armengol, A. Suarez, G. Heredia, A. Ollero, Design, integration and testing of compliant gripper for the installation of helical bird diverters on power lines, in: 2021 Aerial Robotic Systems Physically Interacting with the Environment, IEEE, 2021, pp. 1–8.
[9] K. Klausen, T.I. Fossen, T.A. Johansen, Nonlinear control of a multirotor UAV with suspended load, in: 2015 International Conference on Unmanned Aircraft Systems, ICUAS, 2015, pp. 176–184.
[10] P. Kotaru, K. Sreenath, Multiple quadrotors carrying a flexible hose: dynamics, differential flatness and control, IFAC-PapersOnLine 53 (2) (2020) 8832–8839.
[11] Z. Samadikhoshkho, S. Ghorbani, F. Janabi-Sharifi, Modeling and control of aerial continuum manipulation systems: A flying continuum robot paradigm, IEEE Access 8 (2020) 176883–176894.
[12] P. Tempel, Dynamics of Cable-Driven Parallel Robots with Elastic and Flexible, Time-Varying Length Cables, Fraunhofer Verlag, Stuttgart, 2019.
[13] R. Miyazaki, H. Paul, T. Kominami, K. Shimonomura, Wire-suspended device control based on wireless communication with multirotor for long reach-aerial manipulation, IEEE Access 8 (2020) 172096–172104.
[14] P. Schlott, O. Sawodny, Decoupling control for a gantry crane with an actuated load, in: 2012 7th IEEE Conference on Industrial Electronics and Applications, ICIEA, 2012, pp. 1610–1615.
[15] C.K. Liu, D. Negrut, The role of physics-based simulators in robotics, Ann. Rev. Control Robot. Autonomous Syst. 4 (1) (2021) 35–58.
[16] N. Koenig, A. Howard, Design and use paradigms for gazebo, an open-source multi-robot simulator, in: 2004 International Conference on Intelligent Robots and Systems, Vol. 3, 2004, pp. 2149–2154 vol.3.
[17] J. Cacace, S.M. Orozco-Soto, A. Suarez, A. Caballero, M. Orsag, S. Bogdan, G. Vasiljevic, E. Ebeid, J.A.A. Rodriguez, A. Ollero, Safe local aerial manipulation for the installation of devices on power lines: AERIAL-CORE first year results and designs, Appl. Sci. 11 (13) (2021) 6220.
[18] M. Di Castro, L.R. Buonocore, M. Ferre, S. Gilardoni, R. Losito, G. Lunghi, A. Masi, et al., A dual arms robotic platform control for navigation, inspection and telemanipulation, in: 16th International Conference on Accelerator and Large Experimental Control Systems, Barcelona, Spain, 2017, pp. 8–13.
[19] G. D'Ago, M. Lefebvre, L.R. Buonocore, F. Ruggiero, M. Di Castro, V. Lippiello, Modelling and control of a variable-length flexible beam on inspection ground robot, in: 2022 International Conference on Robotics and Automation, ICRA, IEEE, 2022, pp. 8224–8230.
[20] J. Lee, R. Balachandran, Y.S. Sarkisov, M. De Stefano, A. Coelho, K. Shinde, M.J. Kim, R. Triebel, K. Kondak, Visual-inertial telepresence for aerial manipulation, in: 2020 IEEE International Conference on Robotics and Automation, 2020, pp. 1222–1229.
[21] Z. Ouyang, R. Mei, Z. Liu, M. Wei, Z. Zhou, H. Cheng, Control of an aerial manipulator using a quadrotor with a replaceable robotic arm, in: 2021 IEEE International Conference on Robotics and Automation, 2021, pp. 153–159.
[22] T. Bartelds, A. Capra, S. Hamaza, S. Stramigioli, M. Fumagalli, Compliant aerial manipulators: Toward a new generation of aerial robotic workers, IEEE Robot. Autom. Lett. 1 (1) (2016) 477–483.
[23] A. Suarez, G. Heredia, A. Ollero, Design of an anthropomorphic, compliant, and lightweight dual Arm for aerial manipulation, IEEE Access 6 (2018) 29173–29189.
[24] G. Loianno, V. Spurny, J. Thomas, T. Baca, D. Thakur, D. Hert, R. Penicka, T. Krajnik, A. Zhou, A. Cho, et al., Localization, grasping, and transportation of magnetic objects by a team of mavs in challenging desert-like environments, IEEE Robot. Autom. Lett. 3 (3) (2018) 1576–1583.
[25] M. Mohammadi, D. Bicego, A. Franchi, D. Barcelli, D. Prattichizzo, Aerial telemanipulation with passive tool via parallel position/force control, Appl. Sci. 11 (19) (2021).
[26] K.-S. Hong, U.H. Shah, Dynamics and Control of Industrial Cranes, Springer, 2019.
[27] C. Gabellieri, Y.S. Sarkisov, A. Coelho, L. Pallottino, K. Kondak, M.J. Kim, Compliance control of a cable-suspended aerial manipulator using hierarchical control framework, in: 2020 International Conference on Intelligent Robots and Systems, 2020, pp. 7196–7202.
[28] R. Miyazaki, R. Jiang, H. Paul, Y. Huang, K. Shimonomura, Long-reach aerial manipulation employing wire-suspended hand with swing-suppression device, IEEE Robot. Autom. Lett. 4 (3) (2019) 3045–3052.
[29] M.J. Kim, J. Lin, K. Kondak, D. Lee, C. Ott, Oscillation damping control of pendulum-like manipulation platform using moving masses, IFAC-PapersOnLine 51 (22) (2018) 465–470.
[30] R. Lampariello, J. Heindl, R. Koeppe, G. Hirzinger, Reactionless control for two manipulators mounted on a cable-suspended platform, in: 2006 International Conference on Intelligent Robots and Systems, 2006, pp. 91–97.
[31] H. Osumi, M. Saitoh, Control of a redundant manipulator mounted on a base plate suspended by six wires, in: 2006 International Conference on Intelligent Robots and Systems, 2006, pp. 73–78.

[32] Y.S. Sarkisov, M. Jun Kim, A. Coelho, D. Tsetserukou, C. Ott, K. Kondak, Optimal oscillation damping control of cable-suspended aerial manipulator with a single IMU sensor, in: 2020 IEEE International Conference on Robotics and Automation, 2020, pp. 5349–5355.
[33] R. Featherstone, Rigid Body Dynamics Algorithms, Springer, 2014.
[34] C.D. Santina, R.K. Katzschmann, A. Bicchi, D. Rus, Model-based dynamic feedback control of a planar soft robot: trajectory tracking and interaction with the environment, Int. J. Robot. Res. 39 (4) (2020) 490–513.
[35] R.K. Katzschmann, C.D. Santina, Y. Toshimitsu, A. Bicchi, D. Rus, Dynamic motion control of multi-segment soft robots using piecewise constant curvature matched with an augmented rigid body model, in: 2019 2nd IEEE International Conference on Soft Robotics, 2019, pp. 454–461.
[36] J. Collins, S. Chand, A. Vanderkop, D. Howard, A review of physics simulators for robotic applications, IEEE Access 9 (2021) 51416–51431.
[37] C. Gaz, M. Cognetti, A. Oliva, P. Robuffo Giordano, A. De Luca, Dynamic identification of the franka emika panda robot with retrieval of feasible parameters using penalty-based optimization, IEEE Robot. Autom. Lett. 4 (4) (2019) 4147–4154.
[38] C. Gaz, F. Flacco, A. De Luca, Identifying the dynamic model used by the KUKA LWR: A reverse engineering approach, in: 2014 IEEE International Conference on Robotics and Automation, 2014, pp. 1386–1392.

Giancarlo D'Ago received the B.Sc. degree in automation engineering from the University of Naples "Federico II" in 2018 and the M.Sc.Eng. degree in automation engineering from the University of Naples "Federico II" in 2021. He is currently pursuing the Ph.D. degree with CERN, affiliated with PRISMALab laboratory of University of Naples, in Information Technology and Electrical Engineering. In 2021, he joined CERN's Mechatronics, Robotics, and Operations Section as a Stagiaire, working on the modelling and control of a dual-arm cable-suspended robotic platform for inspection and maintenance in hazardous environments. His research interests include dynamic manipulation, ultra-redundant non-rigid robotics, control of cable-suspended and long-reach robotic platform.